Computational Materials Science 197 (2021) 110592

Contents lists available at ScienceDirect

Computational Materials Science

journal homepage: www.elsevier.com/locate/commatsci

High-throughput computational screening of cathode materials for Li-O_2 battery

A.O. Boev, S.S. Fedotov, K.J. Stevenson, D.A. Aksyonov *

Center for Energy Science and Technology, Skolkovo Institute of Science and Technology, Nobel str.3, 121205 Moscow, Russia

ARTICLE INFO

Keywords:
High-throughput computational screening
Li-air batteries
DFT calculations
Surface energies
Adsorption energies

ABSTRACT

Despite the tremendous specific energy of Li-O_2 energy storage technology in theory, the practically achieved values are still inferior to compete with conventional Li-ion batteries. A key limitation is the inability to use thick gas diffusion electrodes made of carbonaceous materials because of the passivation by discharge products. In this study, a computational methodology for searching alternative positive electrode (cathode) materials for Li-O_2 batteries based on density functional theory is proposed. The methodology includes a three-stage screening with a sequential selection of the best candidates according to their stability, band gap (electronic conductivity), normalized surface energies (stability in a highly porous form), and oxygen adsorption energies (resistance towards oxidation and passivation). The methodology is applied for the A_xB_y series of binary compounds with A = Ti, V, Cr, Mn, Fe, Co, Ni, Cu, Zn, Y, Zr, Nb, Mo, Ru, Ag, Mg, Al and B = B, C, N, O, Si, S and benchmarked with graphite. As a result, 33 potential compounds with low normalized surface energies are identified out of 2800 initial structures taken from the material database. It is shown that only several oxides can be stable towards surface oxidation among the selected compounds and thus considered as potential cathode materials.

1. Introduction

Lithium-Air (Li-O_2) batteries (LABs) have attracted significant attention in recent years due to their much higher theoretical specific energy than that for conventional intercalation-based Li-ion batteries (LIBs) [1,2]. The superior specific energy of LABs is achieved by employing a much lighter cathode - O_2 gas. If O_2 is taken from the ambient atmosphere, the cathode in this battery architecture can be considered nominally weightless in a fully charged state, resulting in a tremendous theoretical specific energy of 11 680 Wh/kg. During discharge, the capture of O_2 reduces the specific energy to 3460 Wh/kg with effective values of around 7000 Wh/kg [3]. The inclusion of a gas diffusion cathode, required for LABs, has only a minor influence on the theoretical estimates of the specific energy due to its very low density. Meanwhile, specific capacities of typical gas cathodes given in literature (851–5813 mAh/g [4,5]) are far beyond that of intercalation-based cathodes (<200 mAh/g) [6].

Despite this advantage, the specific energy of a practical LAB on a cell level is only 100–200 Wh/kg, which is lower than that of commercially available LIBs. This inconsistency appears from a strong dependence of the cathode specific capacity on its thickness. Indeed, it turns out that high specific capacities are measured for very thin electrodes (50 μm), while thicker electrodes are passivated and overgrown by the main and parasitic reaction products from the side of the gas phase input, resulting in the termination of the discharge process [7]. Therefore, even primary LABs are not applicable from a practical standpoint. However, if the problem of the premature electrode passivation can be solved, the practical specific energies of LAB cells can easily achieve 600–800 Wh/kg, doubling that of the best LIB [8,7].

The majority of proposed cathodes are made from carbon-based materials with optional catalytic additives [9]. To name a few, highly porous graphite, paper, wood, fullerenes, soot coated carbon nanotubes, aerogel graphene are typically employed as cathode materials in LABs [9]. However, the high porosity of gas diffusion electrodes enables using heavy elements in their composition without noticeably sacrificing the overall specific energy [7]. Therefore, identifying alternative materials that would be resistant to passivation with discharge products presents an important milestone in the development of practically viable Li-O_2 batteries.

Indeed, in the last few years, the search for carbon-free materials for cathode has gained more momentum, however, the task is challenging. An alternative cathode material should satisfy a specific combination of unique properties: high electrical conductivity, stability in a highly porous form, oxidation resistance, catalytic activity, and resistance to

* Corresponding author.

https://doi.org/10.1016/j.commatsci.2021.110592
Received 31 March 2021; Received in revised form 9 May 2021; Accepted 10 May 2021
Available online 4 June 2021

passivation by discharge and parasitic products [10]. One of the potential alternative materials for cathode was titanium carbide [11]. However, it appeared to be prone to surface oxidation [12]. Cui et al. proposed a carbon-free electrode with a free-standing Co_3O_4 catalyst directly on a nickel foam (Co_3O_4@Ni), which showed a lower overpotential, higher specific capacity, and less capacity fading than the conventional carbon-supported Co_3O_4 [13]. Wang et al. used $FeCo_2O_4$ on a Ni foam ($FeCo_2O_4$@Ni) as a carbon-free cathode, which demonstrated a higher discharge capacity with a lower overpotential compared to the carbon-based $FeCo_2O_4$/Ni (0.84 V vs 1.02 V) [6]. Alternatively to oxides, boron carbide B_4C nanowires were also proposed as a cathode, demonstrating a higher stability (250 cycles) compared to carbon nanotubes (120 cycles) and titanium carbide (8 cycles) [14]. The two-dimensional materials for the cathode hold great potential since they can significantly increase the accessible surface area, reduce ion migration path lengths, and facilitate reaction kinetics. For example, Asadi et al. presented a cathode system based on MoS_2 nanoflakes, which showed an outstanding cyclability (750 cycles with only a 6.5% loss in current density) in comparison with the carbon-based cathodes [15].

Despite the significant progress in the field, several disadvantages of the proposed carbon-free cathode materials, such as complicated synthesis, high overpotentials, and excessive passivation by discharge products, require further development. The promising candidates can be expected in the groups of 2D nanolayered compounds, oxides, nitrides, and silicides.

One of the prospective ways to discover new materials is to use high-throughput computational screening (HTS) [16–20]. For example, Kahle et al. performed a computational screening of solid-state electrolytes and identified five compounds with high ionic conductivity out of 1400 options [21]. Kim et al. used HTS to find active cathodes and inactive stabilizing agents in the Li_2MO_3 class of Li-rich oxides [22], Kirklin et al. - to find new Li-ion battery anode materials [23], while Greely et al. - to find new electrocatalytic materials for hydrogen evolution reaction [24]. Also, the HTS approach facilitated the development of several materials databases: Materials Project (MP) [25], Automatic FLOW for Materials Discovery database (AFLOW) [26–28], Open Quantum Materials Database (OQMD) [29], Crystalium [30], and Joint Automated Repository for Various Integrated Simulations (JARVIS) [31].

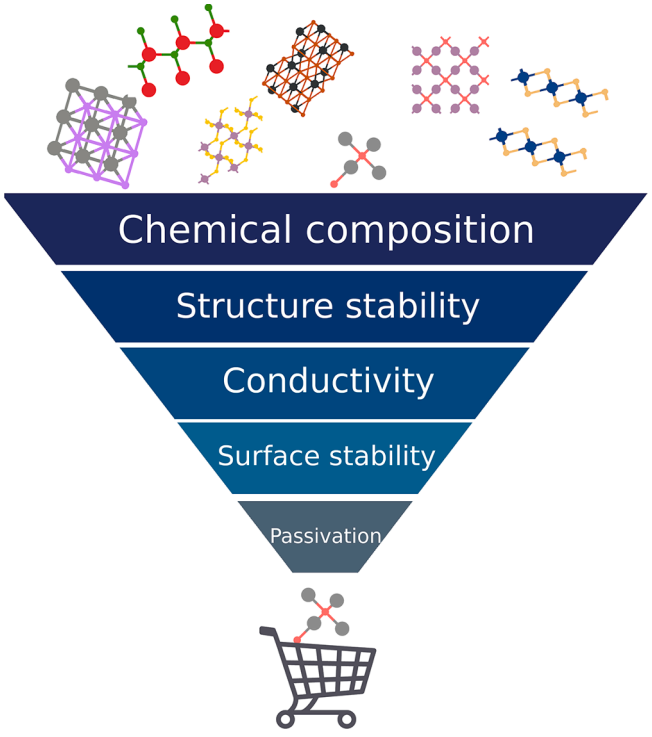

Fig. 1. Schematic representation of the screening funnel used for identification of promising Li-O_2 cathode materials.

In this study, we propose a methodology for high-throughput computational screening of positive gas diffusion electrode materials. The methodology is based on a three-stage screening with a sequential selection of the best candidates according to a specific set of properties. The initial crystal structures are retrieved from experimental and computational repositories (Materials Project in our case) for given chemical compositions. At the first stage, the basic properties, such as price, stability, and a band gap used as a descriptor of electronic conductivity, are extracted from the databases. At the second stage, the specific surface energies are calculated by DFT in a high-throughput manner and used as a descriptor of material's stability in a highly porous form. At the third stage, the resistance towards oxidation and passivation is estimated from the calculated oxygen adsorption energies. The methodology is applied to a wide range of binary compounds and allows to identify several compounds such as VO_2 and $NiSi_2$ as a possible alternative for carbon-free air cathodes in Li-O_2 battery.

In Section 2, we provide details of DFT calculations; in Section 3, we describe the HTS methodology and results of DFT calculations at the second and third stages and then finalize with a discussion and conclusions in Sections 4 and 5, respectively.

2. Methods

The DFT calculations were performed by the pseudopotential plane-wave method, using the VASP code [32]. We used spin-polarized generalized gradient approximation (GGA) implemented by Perdew, Burke, and Ernzerhof for the exchange–correlation energy functional [33]. The energy cutoff was selected to be 400 eV, and the k-spacing parameter was set to 0.2 $Å^{-1}$. To eliminate Pulay errors, the lattice shape and atomic positions optimization (ISIF = 4) was performed at a constant volume for several contracted and expanded cells (11 points) using the quasi-Newton algorithm. The maximum force after optimization was less than 0.05 eV/Å. All calculations were done with the help of the SIMAN software package, which allows to perform VASP calculations in a high-throughput manner [34].

All slabs in the study were constructed using the Pymatgen class `SlabGenerator` [30,35] through `create_surface()` function in the SIMAN package. The function allows setting the facet type, size of the vacuum layer, and slab thickness. A vacuum region of about 15 Å was added along the z-direction to avoid spurious effects stemming from the periodic boundary condition. To guarantee the accuracy in the Fermi energy alignments a dipole correction along z-direction (normal to the surface) was used [35]. The Wulff shape [36] construction was performed by using the WulffShape function implemented in the Pymatgen package [30].

The cohesive energy of a two-component phase A_xB_y was calculated as:

$$E_{\text{coh}} = \frac{E_{A_xB_y} - (xE_A + yE_B)}{x + y} \quad (1)$$

where $E_{A_xB_y}$ is the total energy of the A_xB_y bulk unit cell, $E_{A,B}$ is the energy of the isolated atoms A and B respectively.

For considered stoichiometric surfaces, the surface energy, E_{suf}, was calculated as:

$$E_{\text{suf}} = \frac{E_{\text{tot}} - E_{\text{bulk}}}{2A} \quad (2)$$

where E_{tot} is the total energy of the supercell with two surfaces, E_{bulk} is the total energy of the bulk material with the same number of atoms, and A is the surface area. Both symmetric and non-symmetric (for non-centrosymmetric polar groups) slabs were used for surface energy calculations. Therefore, in the latter case, only the average surface energy

of two non-equivalent surfaces was determined. The convergence of surface energy was reached for five layers. For some compounds, the considered number of surface orientations (3–5) is not enough to construct the true Wulff shape, however, it is sufficient to establish the anisotropy of the surface energy.

To evaluate the resistance of the surface to oxidation, we calculated the adsorption energy of atomic oxygen. To find non-equivalent adsorbate sites on the surface, we used the `AdsorbateSiteFinder` module [37]. We added an oxygen atom at the adsorbate site using the `create_ads()` function of SIMAN.

The oxygen adsorption energy was calculated as:

$$E_{ads} = E_{slab-O} - (E_{slab} + \frac{1}{2}E_{O_2}) \quad (3)$$

where E_{slab-O} is the total energy of the slab with the adsorbed oxygen atom, E_{slab} is the total energy of pure slab and E_{O_2} is the energy of the isolated O_2 molecule. To overcome O_2 overbinding error of DFT, a constant shift of –1.36 eV per O_2 can be applied to adsorption energies [38]. However, it was shown that this correction is appropriate only for binary *s*-oxides [39]. Therefore, the adsorption energies in this study are reported without any corrections.

3. Results

3.1. High-throughput computational screening methodology of cathode compounds

The schematic representation of the screening process is shown in Fig. 1. At the first stage, given the chosen general chemical formula and list of elements, all suitable compounds, their crystal structures, and available properties are retrieved from the computational and experimental materials databases. The following properties are used to select appropriate candidates for the second stage: price, toxicity, energy above the hull, electronic bandgap, and unit cell size. A zero energy above the convex hull indicates the most stable polymorph for a given composition, which is a general requirement for any material. The electronic bandgap serves as a simple descriptor of electronic conductivity. The bandgap criteria can be tuned to select materials with a metallic type of conductivity or small gap semiconductors, where the electronic conductivity can be achieved by doping/defects. The control of the unit cell size is important since for large unit cells the resulting slabs necessary for the surface calculations might require much computational time.

At the second stage, the materials that should be stable in a highly porous form are selected. To achieve this, we propose a new descriptor - the ratio between cohesive energy and surface energy E_{coh}/E_{suf}. Indeed, the material to be suitable for application as a cathode should be synthesized with a very large specific surface area and have numerous continuous pores available for electrolyte penetration. This would be possible only in the case of relatively stable free surfaces, i.e. those with low formation energies. Otherwise, the material will tend to reduce its surface by coalescence of the structure. However, due to the largely varying bonding strength of materials, the surface energy is not solely sufficient to select the best candidate out of multiple variants. Therefore, the aforementioned ratio E_{coh}/E_{suf} should be used. The materials with the best E_{coh}/E_{suf} ratios are selected for further consideration. Also, the anisotropy of the surface energy should be taken into account, which is achieved by calculating energies for a set of surfaces required for the construction of a closed Wulff shape.

At the third stage, the oxidation resistance is estimated by calculating the adsorption of the atomic oxygen on the most stable surfaces and comparing it to that on graphite. At this point, it is difficult to judge about optimal values of oxygen adsorption energies. However, too negative values would mean a strong tendency for oxidation, while positive energies may prevent oxygen redox reactions. To estimate the

Table 1
List of chosen materials with general formula A_xB_y with their symmetry groups (SG) and calculated cohesive energies (in eV).

Material	SG symbol	E_{coh}	Material	SG symbol	E_{coh}
	cubic			trigonal	
Ag_2O	$Pn\bar{3}m$	2.90	B_2Mo	$R\bar{3}m$	6.85
CoN	$F\bar{4}3m$	5.18	Cr_2N	$P\bar{3}1m$	4.80
CoO	$F\bar{4}3m$	5.05	CrS_2	$P\bar{3}m1$	4.04
CoSi	$P2_13$	5.58	MgS_2	$R\bar{3}m$	3.51
$CoSi_2$	$Fm\bar{3}m$	5.32	MnS_2	$R\bar{3}m$	4.00
Cr_3Si	$Pm\bar{3}n$	4.53	Nb_2N	$P\bar{3}1m$	7.40
Cu_2O	$Pn\bar{3}m$	3.87	Ti_2O	$P\bar{3}m1$	6.60
Fe_3Si	$Fm\bar{3}m$	5.35	TiS_2	$R\bar{3}m$	5.25
FeN	$F\bar{4}3m$	5.31	Y_2C	$R\bar{3}m$	5.83
FeSi	$P2_13$	5.40	Zr_3O	$R\bar{3}c$	7.06
Mg_2Si	$Fm\bar{3}m$	2.70	ZrS_2	$P\bar{3}m1$	5.81
Mn_3Si	$Fm\bar{3}m$	4.38		tetragonal	
Mn_4N	$Pm\bar{3}m$	4.31	Cr_2B	$I4/mcm$	5.20
MnN	$F\bar{4}3m$	4.72	CrB	$I4_1/amd$	5.75
MnSi	$P2_13$	4.71	$CrSi_2$	$I4/mmm$	4.79
$NiSi_2$	$Fm\bar{3}m$	5.05	CuO	$P4_2/mmc$	4.04
$SiMo_3$	$Pm\bar{3}n$	6.27	Fe_2B	$I4/mcm$	5.89
$SiNi_3$	$Pm\bar{3}m$	5.26	Fe_8N	$I4/mmm$	5.19
SiRu	$P2_13$	6.28	FeB	$I4_1/amd$	6.17
TiC	$Fm\bar{3}m$	7.50	FeS	$P4/nmm$	4.72
TiN	$Fm\bar{3}m$	7.02	Mn_2B	$I4/mcm$	5.12
V_3Si	$Pm\bar{3}n$	5.68	MoB	$I4_1/amd$	6.91
YN	$Fm\bar{3}m$	6.45	$MoSi_2$	$I4/mmm$	5.70
YS	$Fm\bar{3}m$	5.77	Ni_2B	$I4/mcm$	5.68
ZrC	$Fm\bar{3}m$	8.24	RuO_2	$P4_2/mnm$	5.51
ZrN	$Fm\bar{3}m$	7.53	Ti_2N	$P4_2/mnm$	6.69
	monoclinic		VO_2	$P4_2/mnm$	6.40
Ag_2S	$P2_1$	2.80	Zr_2N	$P4_2/mnm$	7.24
AgO	$C2/c$	3.07	Zr_2Si	$I4/mcm$	6.56
FeO	$C2/m$	5.18	ZrS	$P4/nmm$	6.27
NiS_2	$P2_1/c$	4.04		hexagonal	
ZrS_3	$P2_1/m$	5.20	CrN	$P\bar{6}m2$	5.14
	orthorhombic		Fe_3N	$P6_322$	5.25
Co_2N	$Pnnm$	5.23	MgB_2	$P6/mmm$	4.92
CoB	$Pnma$	6.28	MoC	$P\bar{6}m2$	7.27
CrB_4	$Immm$	6.25	MoS_2	$P6_3/mmc$	5.15
FeS_2	$Pnnm$	4.39	NbB_2	$P6/mmm$	7.37
MnB	$Pnma$	5.65	NbN	$P\bar{6}m2$	7.31
Nb_3B_4	$Immm$	7.49	NbS_2	$P6_3/mmc$	5.57
NbB	$Cmcm$	7.54	$NbSi_2$	$P6_222$	5.99
Ni_3O_4	$Cmmm$	4.83	Ni_3N	$P6_322$	4.92
NiB	$Cmcm$	5.89	TiB_2	$P6/mmm$	7.16
NiSi	$Pnma$	5.22	TiO	$P\bar{6}2m$	7.00
Ti_3B_4	$Immm$	6.94	TiS	$P\bar{6}m2$	5.82
TiB	$Pnma$	6.77	VB_2	$P6/mmm$	6.68
TiSi	$Pnma$	5.81	VN	$P\bar{6}m2$	6.47
$TiSi_2$	$Cmcm$	5.46	VS_2	$P6_3/mmc$	4.83
V_3B_4	$Immm$	6.80	VSi_2	$P6_222$	5.36
VB	$Cmcm$	6.75	YB_2	$P6/mmm$	6.28
YSi	$Cmcm$	5.31	ZnO	$P6_3mc$	3.72
ZrSi	$Pnma$	6.42	ZrB_2	$P6/mmm$	7.41
$ZrSi_2$	$Cmcm$	5.85			

Table 2
Compounds with non-zero bandgap values calculated by DFT [25].

Material	Ag_2S	CoO	Cu_2O	FeO	FeS_2	FeSi	Mg_2Si	MgS_2	MoS_2	Ni_3O_4	NiS_2	SiRu	TiS_2	VO_2	YN	ZnO	ZrS_2	ZrS_3
Bandgap, eV	1.33	0.59	0.50	1.27	0.88	0.17	0.24	0.92	1.78	0.40	0.20	0.23	0.02	0.89	0.15	0.73	1.05	1.10

resistance to passivation by discharge products, the interface energy of the cathode/discharge product pair (e.g. cathode/LiO_2) is calculated. The materials with positive or near zero interface energies would be entirely resistant for surface passivation, while highly negative energies imply a strong tendency to passivation. The calculation of interface energies with DFT in a high-throughput manner is the most challenging part of the methodology and is not included in the current study and will be published elsewhere. However, our preliminary results show that oxygen adsorption energy can also be used to estimate material tendency toward passivation with lithium superoxide.

The HTS methodology of screening is implemented into the package SIMAN [34], which automates the generation of input codes for DFT, batch submission of jobs, extraction of results in a structured representation, and their subsequent analysis. An example of the query script used for retrieving structures from the Materials Project database is provided in Supplementary material.

3.2. Application of HTS methodology for cathode materials screening

3.2.1. Chosen compounds

We apply the proposed methodology to compounds with the general formula of A_xB_y, where A and B are metals and non-metals, respectively. Using general chemical and economic considerations, we select Ti, V, Cr, Mn, Fe, Co, Ni, Cu, Zn, Y, Zr, Nb, Mo, Ru, Ag, Mg, Al in place of A and B, C, N, O, Si, S in place of B. Metallic components included 3d metals, 4d metals plus Mg and Al, excluding Rh and Pd due to their high price (see element prices in Table S1.1), Tc due to its synthesis difficulties and radioactivity [40], and Cd due to its toxicity. As a primary database, we employed the Materials Project database, which returned 2755 compounds.

After excluding all unstable compounds ('e_above_hull' $>$ 0.005 eV (only one compound with the lowest energy was used), non-conductive compounds ('band_gap' $>$ 2 eV) and compounds with a larger unit cell ('nsites' $>$ 10 atoms), the number of compounds successively reduced to 242, 230, and 110, respectively. Finally, we removed 11 compounds known to be dangerous, hydrophobic, or exist in a narrow temperature range. After the first stage, the resulting list of potential cathodes contained 99 entries (Table 1). Only 18 of them have a non-zero DFT calculated bandgap value (Table 2).

3.2.2. Surface stability

To estimate the surface stability of the selected materials in a highly porous form, we calculated E_{coh}/E_{suf} ratios. The cohesive energies for 99 compounds are provided in Table 1 and Fig. S1.1 in Supplementary. As expected from general considerations, carbides, borides, and nitrides have the highest cohesive energies, which grow on increasing a non-metal fraction from A_2B to AB_2 (Table S1.2). In contrast to that, silicides and sulfides with higher non-metal fractions are characterized with the lower E_{coh} values.

To identify the lowest-energy surfaces several candidates with small indices have been taken depending on the crystal system using the Crystalium database [30]: cubic - (110), (111), (001); monoclinic - (001), (110), (111); trigonal - (102), (111), (001); tetragonal - (001), (101), (100); orthorhombic - (001), (110), (111); hexagonal - (001), (110), (10–1). The sufficiency of the chosen surfaces was tested for several compounds by including more crystal orientations. In particular, we additionally considered (100) and (104) surfaces for trigonal, (104) for orthorhombic, and (211) and (311) for cubic and tetragonal systems (see Tables S2.1-S2.6). The analysis of Wulff shapes showed that the contribution of the newly added surfaces is small and has only a minor influence on the Wulff shape. Additionally, for each orientation, we considered all non-equivalent terminations, whose energies can vary significantly. For example, the energies of Nb and B terminations for NbB_2 (10–1) are 4.04 and 1.85 J/m^2, respectively (Fig. S2.1). The calculated surface energies for the most stable terminations and three representative surface orientations are collected in Fig. 2 for 99 compounds. The Wulff shapes with numerical data are given in Tables S2.1-S2.6. In most cases, the Wulff shapes correlate with the morphology of crystals/particles of this compound.

The analysis of surface energies allows drawing several conclusions. Firstly, the surface energy is mainly defined by the non-metal component, while the influence of the metal one in many cases is of secondary importance (Figs. S2.4 and S2.5). Secondly, the strong anisotropy of the surface energies is observed for layered materials (see Wulff shape in Fig. S2.2), especially for sulfides and some oxides, while other compounds reveal relatively isotropic energies (Fig. S2.5, left). The strong surface energy anisotropy of the layered compounds can be compared to that of graphite, which has 0.02 and 4.89–6.38 J/m^2 energies for basal (0001) and prismatic (10–10) surfaces, respectively.

Noteworthy, the surface energies set the same trend as cohesive energies. In most cases, these are largest for carbides/borides and smallest for sulfides (Fig. S2.5). Some exceptions from this trend are presented by cubic TiC, ZrC, and trigonal Y_2C phases. Also, some hexagonal nitrides show higher surface energies compared to borides. Overall, the surface energy alone poorly suits as a criterion for surface stability comparison across different compounds. Therefore, the E_{coh}/E_{suf} ratio (further referred to as specific area) was calculated. Physically, it shows how much surface area can be formed at the cost of cohesive energy. A larger value corresponds to an easier formation of a surface for a particular material irrespective of its cohesive strength. The E_{coh}/E_{suf} ratio is shown in Fig. 3 as a function of E_{suf}. It is seen that compounds with the same E_{suf} can have quite different specific areas, e.g. at E_{suf}=0.5 J/m^2 the areas vary from 100 to 300 Å^2. At this moment, it is difficult to conclude which value of the specific area is needed for the material to serve as an air cathode (see Discussion 4). Therefore, for the next stage, we arbitrarily set a $E_{coh}/E_{suf} > 70$ Å^2 criterion, which gives 33 compounds with the most stable surfaces (highlighted in green in Tables S2.1-S2.6).

3.2.3. Surface tendency to oxidation

To establish a tendency of surface oxidation and passivation by discharge products we calculated oxygen adsorption energies for 33 selected compounds. The top adsorption positions for the two lowest-energy surfaces, determined from the Wulff shapes, were considered. The calculated energies in comparison to that in graphite are presented in Fig. 4. The surface structure and adsorption positions are provided in Tables S3.1-S3.6.

We identify three types of behavior depending on the sign of adsorption energies at the two lowest energy surfaces. Looking at graphite, the adsorption energies at (0001) and (10–10) surfaces are drastically different (1.16 eV vs –4.5 eV), which should have a large impact on the oxidation behavior of this material. It can be assumed that the prismatic surface (10–10) can be easily oxidized and passivated by discharge products, while (0001) should be much more stable. A similar behavior is observed for VO_2, RuO_2, Ag_2O and AgO, where the basal surfaces demonstrate positive adsorption energies, while the prismatic surfaces are prone to oxidation.

In contrast, copper oxides (Cu_2O and CuO) and silver sulfide Ag_2S display positive adsorption energies at both lowest-energy surfaces, which makes them highly resistant towards oxidation and passivation.

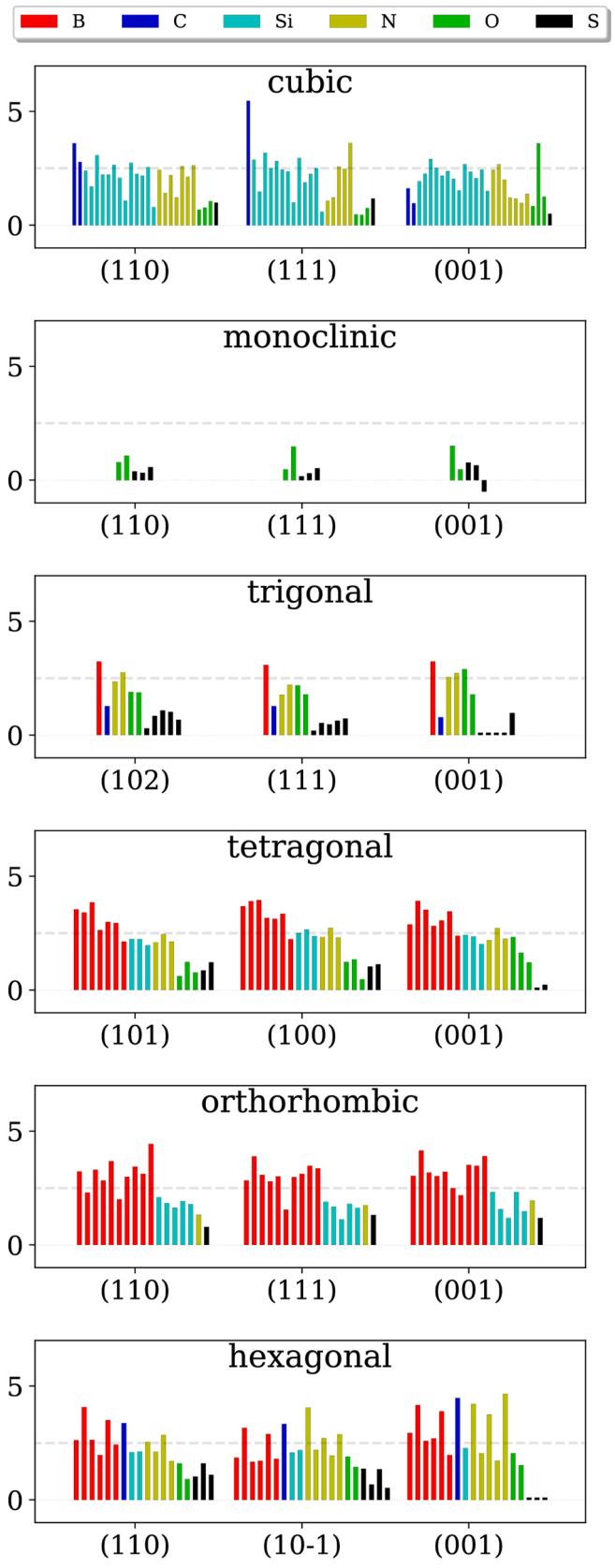

(caption on next column)

Fig. 2. Surface energies (J/m^2) grouped by crystal system for considered compounds in accordance with the bar position: cubic - TiC, ZrC, CoSi, $CoSi_2$, Cr^3Si, Fe_3Si, FeSi, Mn_3Si, MnSi, $NiSi_2$, Mo_3Si, Ni_3Si, RuSi, V_3Si, Mg_2Si, CoN, FeN, Mn_4N, MnN, TiN, YN, ZrN, Ag_2O, CoO, Cu_2O, YS; monoclinic - AgO, FeO, Ag_2S, NiS_2, ZrS_3; trigonal - MoB_2, Y_2C, Cr_2N, Nb_2N, Ti_2O, Zr_3O, CrS_2, MnS_2, TiS_2, ZrS_2, MgS_2; tetragonal - MoB, Cr_2B, CrB, Fe_2B, FeB, Mn_2B, Ni_2B, $CrSi_2$, $MoSi_2$, Zr_2Si, Fe_8N, Ti_2N, Zr_2N, CuO, RuO_2, VO_2, FeS, ZrS; orthorhombic - CoB, CrB_4, MnB, Nb_3B_4, NbB, NiB, Ti_3B_4, TiB, V_3B_4, VB, NiSi, TiSi, $TiSi_2$, YSi, ZrSi, $ZrSi_2$, Co_2N, FeS_2; hexagonal - NbB_2, TiB_2, VB_2, YB_2, ZrB_2, MgB_2, MoC, $NbSi_2$, VSi_2, CrN, Fe_3N, NbN, Ni_3N, VN, TiO, ZnO, MoS_2, NbS_2, TiS, VS_2.

Finally, all other considered compounds show strong oxygen attraction for both lowest-energy surfaces, making them susceptible to oxidation and passivation. Still, the oxygen attraction for 2D sulfides is much weaker than that for the prismatic surface of graphite.

4. Discussion

The proposed screening methodology entirely relies on DFT calculated properties of compounds and has its advantages and shortcomings inherited from the computational method. The main advantage is the possibility to consider a broad spectrum of compounds consistently with the cancellation of inaccuracies. For example, the known tendency of DFT to underestimate surface energies does not prevent identifying the material with the lowest energy since this underestimation is more or less systematic across the whole set of considered materials. Another strong point of the methodology is using materials databases with pre-calculated properties, which significantly narrows down the list of potential candidates after applying a reasonable set of selecting criteria. The disadvantages are related to the inaccurate reproduction of bandgaps, no automated filtering of toxic, hydrophobic, and fragile materials, as well as high computational demands, especially required for estimation of interface energies, where large supercells are needed.

It is well known that the PBE functional used in this study underestimates bandgaps of semiconductors [41]. In some cases, PBE predicts the material to be a metal, while it is known to be a semiconductor experimentally. Therefore, the requirement of slightly positive or even zero bandgaps does not guarantee that selected materials will possess high electronic conductivities. On the other hand, the conductivity can be increased by doping or introducing point defects, making such semiconductors suitable for cathode applications. Semiconductors can possess an optimal combination of properties required for a cathode. Therefore, it is important not to filter them out by setting too strict thresholds on a bandgap. Overall, the accuracy of the bandgap estimation can be straightforwardly improved by single-point calculations at the first stage using hybrid XC functionals. Among 33 selected A_xB_y compounds, only ten compounds have relatively small bandgaps (most of the oxides, sulfides, Mg_2Si, YN), while the rest are metallic conductors. The experimentally measured bandgaps are collected in Table S1.3, which were taken from the 'Bandgap' database [42]). It is also known that some materials are able to demonstrate a metal–semiconductor transition, such as 1T-2H transition in MoS_2 [43] and monoclinic insulator-rutile metal transition in VO_2 at T above 340 K [44,45].

In addition to surface energies, we provide corresponding Wulff shapes (Tables S2.1–2.6), which are expected to determine the morphology of particles in an experiment. The morphology is highly important since certain surfaces may be more relevant due to their higher resistance to passivation and increased catalytic activity. To check the correspondence between the observed morphologies and predicted Wulff shapes, we compared some of our results with the available experimental data and found excellent agreement. For example, the hydrothermally synthesized VO_2 ($P4_2/mnm$) phase reveals pencil-like morphology [46], which aligns well with the rod-like Wulff shape predicted by DFT (see Table S2.6). Layered sulfides are usually synthesized in the form of nanoflakes [47,48], corroborating with their

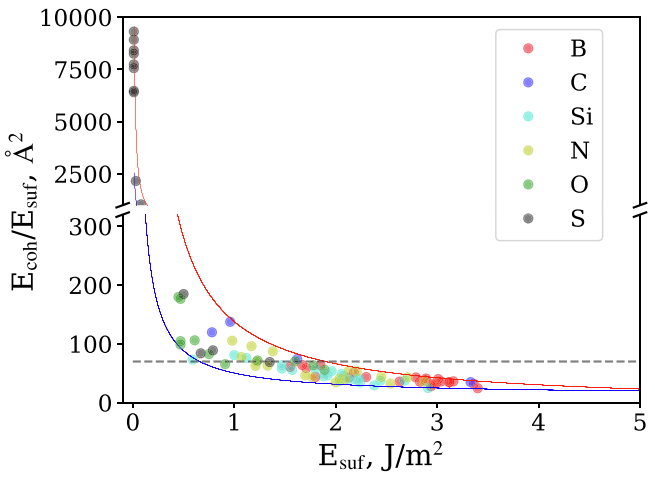

Fig. 3. Ratio E_{coh}/E_{suf} vs. E_{suf} for considered compounds. Dashed line on 70 Å^2 shows criteria for compounds with stable surfaces.

predicted by DFT disk-like Wulff shapes. Another example is Ag_2O whose particles can have different morphologies depending on the synthesis conditions, however, one of the obtained shapes is octahedron [49,50], predicted by DFT as well. Therefore, the Wulff construction is a powerful tool for predicting morphology. In case when the experimentally obtained morphology is different from the prediction, the explanation should be rooted in a surface reconstruction or surface energy modification due to adsorption of some species, such as CO_2 or other by-products of a synthesis.

To estimate the stability of cathode material in a highly porous form, we introduce a new descriptor - a ratio of cohesive and surface energies $S = E_{coh}/E_{suf}$. This is justified by the fact that the correlation between cohesive and surface energies is relatively weak (Fig. S2.3), meaning that E_{suf} can vary in a wide interval for a particular value of E_{coh}. This descriptor has a dimensionality of the area and should correlate with the experimentally measured specific areas of porous materials. The specific area obtained in the experiment strongly depends on the synthesis conditions. However, the possibility to obtain a large specific area and its stability at increased temperatures should be connected with E_{coh}/E_{suf}. Therefore, we have compared experimental data on specific areas with our predictions. For Ag_2O, the S value is 100 Å^2, and indeed many experimental studies show that it can be synthesized in the form of nanoparticles with the average size of 40 nm corresponding to the

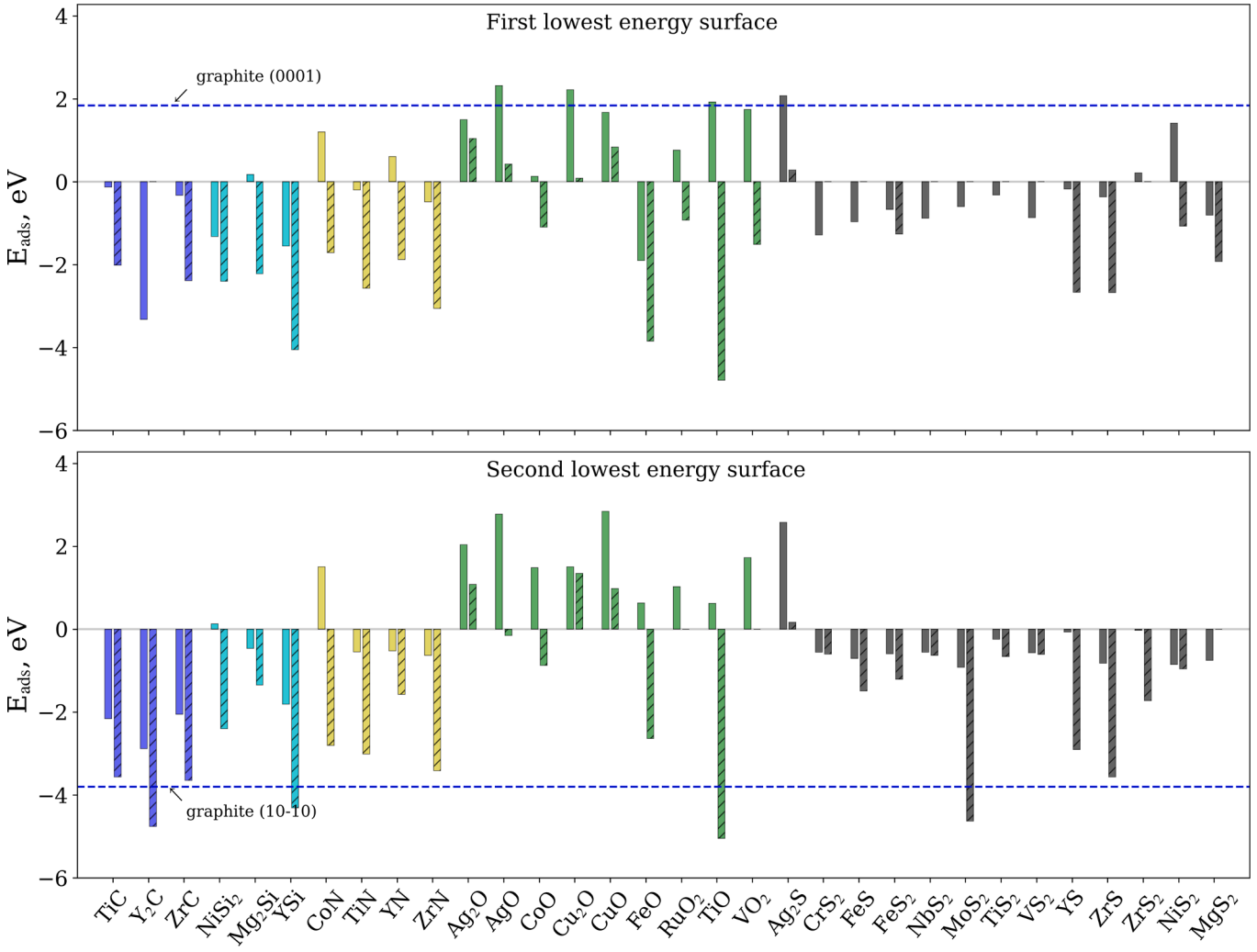

Fig. 4. Adsorption energies of the atomic oxygen on the surfaces of considered compounds, relative to the O_2 molecule. The top panel shows adsorption energies for the lowest energy surface and the blue horizontal line is the oxygen adsorption energy (1.84 eV) at the (0001) graphite surface. The bottom panel shows adsorption energies for the second lowest energy surface and the blue horizontal line is the oxygen adsorption energy (–3.88 eV) at the (10–10) graphite surface. Solid and shaded bars correspond to the weakest and strongest adsorption sites.

specific area of 22 m^2/g [51]. For CuO, the S value is 270 Å^2, and the observed specific areas are 22–143.7 m^2/g with 3–9 nm particles [52,53]. MoS_2, TiS_2 and NbS_2 have extremely large S values (8251 Å^2, 8411 Å^2 and 8924 Å^2, respectively). The average sizes of experimentally obtained 1 nm thick nanosheets are 300–3000 nm with corresponding specific areas of 455–1056 m^2/g [54]. This is significantly larger compared to other materials and close to carbon materials (<900 m^2/g) [15].

Turning to surface oxidation, across oxides, Ag_2O, Cu_2O and CuO are resistant with respect to oxygen adsorption. This is reasonable as the materials are already in their stable oxidation states. The VO_2 and FeO are in their intermediate oxidation states, therefore oxygen adsorption is relatively strong. Even the most stable surface of VO_2, (110) will be oxidized, which is in agreement with previous theoretical investigations of [55] and experimental observations of [56].

Sulfides are even more prone to oxygen adsorption. Among considered sulfides, only Ag_2S has a nearly zero adsorption energy at the most stable surface, while other sulfides strongly adsorb oxygen. Despite the high stability of the basal surface in the case of layered sulfides, they should be easily oxidized in Li-O_2 cell. This is confirmed by several studies, where a formation of the oxide layer was found [57,58].

As for carbides, nitrides, and silicides, they heavily adsorb oxygen, emphasizing easy oxidation in a cell. A prominent example is TiC which was studied in detail as a cathode for Li-air batteries [11], and the formation of an oxide layer was observed [12]. Among this group of compounds, the weakest adsorption is observed for $NiSi_2$. Despite the potential formation of oxide surface layers, they are not necessary of detrimental nature, as it is known that Ni-O oxides may be electronically conductive, which will not block the discharge process. However, in this case, the passivation of Ni-O surface by superoxides will determine the performance of such cathodes.

It turns out that VO_2 [59,60] and CuO [61] from our predicted list were already synthesized as potential carbon-free cathode materials. Asadi et al. [15] obtained that MoS_2 nanoflakes is a promising cathode material for LABs. Huang et al. [62] synthesized a composite aerogel of MoS_2/C as an electrode material for supercapacitors. Another graphene-like layered transition-metal dichalcogenide VS_2 has also been considered as a potential cathode in LABs [63,64].

None of the considered binary compounds fully satisfy the chosen criteria, such as metallic conductivity, stability in highly porous form, and absence of oxygen adsorption. If only the most stable surface is taken into account, then graphite is the only material that meet all the requirements, apparently explaining the huge success of carbon materials in Li-air batteries. If the condition of electronic conductivity is weakened then the best candidates are Ag_2O ($Pn\bar{3}m$), Cu_2O ($Pn\bar{3}m$) and CuO ($P4_2/mnm$). However, all of them have a bandgap of about 1–2 eV (Table S1.3). Thus special measures should be applied to increase the electronic conductivity. If the weak oxygen adsorption is allowed, then the best candidates are VO_2 ($P4_2/mnm$), layered sulfides and $NiSi_2$. The VO_2 ($P4_2/mnm$) is expected to be slowly oxidized to V_2O_5, therefore it might be suitable only for a primary cell. Also, the metallic $P4_2/mnm$ phase of VO_2 should be additionally stabilized at room temperature by, for example, doping with W [65], as in the pure state, it shows a transition into the monoclinic $P2_1/c$ insulating state.

5. Conclusions

In summary, we proposed and developed a methodology for high-throughput computational screening of cathode materials for Li-air batteries. The methodology comprises a sequential selection of compounds that meet the criteria of phase stability, electronic conductivity, surface stability, and oxidation resistance. To estimate the surface stability, a ratio between cohesive and surface energy (S) is introduced as a new descriptor with a physical meaning of a specific surface area. Irrespective of the bond strength, materials with larger S should be easier synthesized in a highly porous form. The resistance to oxidation and passivation by discharge products is estimated from the adsorption energy of atomic oxygen at the most stable surfaces.

We applied our methodology to 2755 A_xB_y binary compounds retrieved from the Materials Project Database and selected 99 compounds with thermodynamically stable crystal structures, which are metals or semiconductors with DFT calculated bandgap less than 2 eV having a unit cell with less than 11 atoms.

For all 99 compounds, we determined the lowest energy surfaces and constructed their Wulff shapes, which should correlate with the morphology of the synthesized particles. The cohesive energies span the range of 2.7–8.2 eV resulting in different S values for materials with similar surface energies. We set S>70 Å^2 criterion, allowing us to select 33 prospective compounds that can be prepared in a highly porous form, which is confirmed by the experimental data.

The calculation of oxygen adsorption energy showed that only oxides have high resistance towards oxidation, which is comparable with the chemically stable (0001) surface of graphite. However, compared to the edge sites available on the prismatic surface (10–10) of graphite, all oxides, sulfides, and even several silicides show much better oxidation resistance.

Among considered materials CuO, $NiSi_2$ and VO_2 look the most promising as alternative carbon-free cathode materials, though neither of them fully met specified criteria. Applying the developed methodology to a broader list of binary and ternary oxides should help identify new cathode materials well-suited for metal-air batteries.

Data Availability Statement

All data generated or analyzed during this study are included in this article and its Supplementary material.

CRediT authorship contribution statement

A.O. Boev: Data curation, Formal analysis, Investigation, Methodology, Software, Visualization, Writing - original draft, Writing - review & editing. **S.S. Fedotov:** Data curation, Formal analysis, Writing - review & editing. **K.J. Stevenson:** Resources, Validation, Writing - review & editing. **D.A. Aksyonov:** Funding acquisition, Conceptualization, Data curation, Formal analysis, Investigation, Methodology, Software, Visualization, Writing - original draft, Writing - review & editing.

Declaration of Competing Interest

The authors declare that they have no known competing financial interests or personal relationships that could have appeared to influence the work reported in this paper.

Acknowledgements

D.A. Aksyonov acknowledges Russian Science Foundation for the financial support of this study (Grant No.19–73-00321).

Appendix A. Supplementary data

Supplementary data associated with this article can be found, in the online version, at https://doi.org/10.1016/j.commatsci.2021.110592.

References

[1] Zhong-Li Wang, Xu Dan, Xu Ji-Jing, Xin-Bo Zhang, Oxygen electrocatalysts in metal-air batteries: from aqueous to nonaqueous electrolytes, Chem. Soc. Rev. 43 (2014) 7746–7786, https://doi.org/10.1039/C3CS60248F.
[2] Alexander Kraytsberg, Yair Ein-Eli, Review on li–air batteries—opportunities, limitations and perspective, J. Power Sources 196 (2011) 886–893, https://doi.org/10.1016/j.jpowsour.2010.09.031.

[3] Simon Clark, Arnulf Latz, Birger Horstmann, A review of model-based design tools for metal-air batteries, Batteries 4 (2018) 5, https://doi.org/10.3390/batteries4010005.

[4] Jie Xiao, Donghai Wang, Wu Xu, Deyu Wang, Ralph Williford, Jun Liu, Ji-Guang Zhang, Optimization of air electrode for li/air batteries, J. Electrochem. Soc. 157 (4) (2010) A487–A492, https://doi.org/10.1149/1.3314375.

[5] S.D. Beattie, D.M. Manolescu, S.L. Blair, Highcapacity lithium-air cathodes, J. Electrochem. Soc. 156 (1) (2008) A44–A47, https://doi.org/10.1149/1.3005989.

[6] Hui Wang, Houzhen Chen, Hongjiao Wang, Wu Lei, Wu Qixing, Zhongkuan Luo, Fang Wang, Hierarchical porous $FeCo_2O_4$@Ni as a carbon- and binder-free cathode for lithium−oxygen batteries, J. Alloy. Compd. 780 (2019) 107–115, https://doi.org/10.1016/j.jallcom.2018.11.231.

[7] Artem V. Sergeev, Alexander V. Chertovich, Daniil M. Itkis, Eugene A. Goodilin, Alexei R. Khokhlov, Effects of cathode and electrolyte properties on lithium-air battery performance: Computational study, J. Power Sources 279 (2015) 707–712, https://doi.org/10.1016/j.jpowsour.2015.01.024.

[8] Girish Girishkumar, Bryan McCloskey, Alan C. Luntz, Sally Swanson, Winfried Wilcke, Lithium-air battery: promise and challenges, J. Phys. Chem. Lett. 1 (2010) 2193–2203, https://doi.org/10.1021/jz1005384.

[9] Zhong Ma, Xianxia Yuan, Lin Li, Zi-Feng Ma, David P. Wilkinson, Lei Zhang, Jiujun Zhang, A review of cathode materials and structures for rechargeable lithium-air batteries, Energy Environ. Sci. 8 (2015) 2144–2198, https://doi.org/10.1039/C5EE00838G.

[10] Chris Tran, Xiao-Qing Yang, Qu Deyang, Investigation of the gas-diffusion-electrode used as lithium/air cathode in non-aqueous electrolyte and the importance of carbon material porosity, J. Power Sources 195 (7) (2010) 2057–2063, https://doi.org/10.1016/j.jpowsour.2009.10.012.

[11] Muhammed M. Ottakam, Stefan A. Thotiyl, Zhangquan Peng Freunberger, Yuhui Chen, Zheng Liu, Peter G. Bruce, A stable cathode for the aprotic Li-O2 battery, Nature Mater. 12 (2013) 1050–1056, https://doi.org/10.1038/nmat3737.

[12] Anna Ya. Kozmenkova, Elmar Yu. Kataev, Alina I. Belova, Matteo Amati, Luca Gregoratti, et al., Tuning surface chemistry of tic electrodes for lithium-air batteries, Chem. Mater. 28 (2016) 8248–8255, https://doi.org/10.1021/acs.chemmater.6b03195.

[13] Yanming Cui, Zhaoyin Wen, Yu Liu, A freestanding-type design for cathodes of rechargeable Li-O2 batteries, Energy Environ. Sci. 4 (2011) 4727–4734, https://doi.org/10.1039/C1EE02365A.

[14] Shidong Song, Wu Xu, Ruiguo Cao, Langli Luo, Mark H. Engelhard, Mark E. Bowden, Bin Liu, Luis Estevez, Chong-Min Wang, Ji-Guang Zhang, B4C as a stable non-carbon-based oxygen electrode material for lithium-oxygen batteries, Nano Energy 33 (2017) 195–204, https://doi.org/10.1016/j.nanoen.2017.01.042.

[15] Mohammad Asadi, Bijandra Kumar, Cong Liu, Patrick Phillips, Poya Yasaei, Amirhossein Behranginia, Peter Zapol, Robert F. Klie, Larry A. Curtiss, Amin Salehi-Khojin, Cathode Based on Molybdenum Disulfide Nanoflakes for Lithium–Oxygen Batteries, ACS Nano 10 (2) (2016) 2167–2175, https://doi.org/10.1021/acsnano.5b06672.

[16] Anubhav Jain, Yongwoo Shin, Kristin A. Persson, Computational predictions of energy materials using density functional theory, Nature Rev. Mater. 1 (2016) 1–13, https://doi.org/10.1038/natrevmats.2015.4.

[17] Juan J. de Pablo, Jackson E. Nicholas, Michael A. Webb, Long-Qing Chen, Joel E. Moore, Morgan Dane, Ryan Jacobs, Tresa Pollock, Darrell G. Schlom, Eric S. Toberer, et al., New frontiers for the materials genome initiative, npj Comput. Mater. 5 (2019) 41, https://doi.org/10.1016/j.cossms.2014.02.003.

[18] Francesco Naccarato, Francesco Ricci, Jin Suntivich, Geoffroy Hautier, Ludger Wirtz, Gian-Marco Rignanese, Searching for materials with high refractive index and wide band gap: A first-principles high-throughput study, Phys. Rev. Mater. 3 (2019), 044602, https://doi.org/10.1103/PhysRevMaterials.3.044602.

[19] Guillaume Brunin, Francesco Ricci, Viet-Anh Ha, Gian-Marco Rignanese, Geoffroy Hautier, Transparent conducting materials discovery using high-throughput computing, npj Comput. Mater. 5 (63) (2019) 1–13, https://doi.org/10.1038/s41524-019-0200-5.

[20] Francesco Ricci, Alexander Dunn, Anubhav Jain, Gian-Marco Rignanese, Geoffroy Hautier, Gapped metals as thermoelectric materials revealed by high-throughput screening, J. Mater. Chem. A 8 (2020) 17579–17594, https://doi.org/10.1039/D0TA05197G.

[21] Leonid Kahle, Aris Marcolongo, Nicola Marzari, High-throughput computational screening for solid-state Li-ion conductors, Energy Environ. Sci. 13 (2020) 928–948, https://doi.org/10.1039/C9EE02457C.

[22] Soo Kim, Muratahan Aykol, Vinay I. Hegde, Zhi Lu, Scott Kirklin, Jason R. Croy, Michael M. Thackeray, Chris Wolverton, Material design of high-capacity Li-rich layered-oxide electrodes: Li_2MnO_3 and beyond, Energy Environ. Sci. 10 (2017) 2201–2211, https://doi.org/10.1039/C7EE01782K.

[23] Scott Kirklin, Bryce Meredig, Chris Wolverton, High-throughput computational screening of new Li-ion battery anode materials, Adv. Energy Mater. 3 (2013) 252–262, https://doi.org/10.1002/aenm.201200593.

[24] Jeff Greeley, Thomas F. Jaramillo, Jacob Bonde, Ib Chorkendorff, Jens K. Nørskov, Computational high-throughput screening of electrocatalytic materials for hydrogen evolution, Nat. Mater 5 (2006) 909–913, https://doi.org/10.1038/nmat1752.

[25] Anubhav Jain, Joseph Montoya, Shyam Dwaraknath, Nils Zimmermann, John Dagdelen, Matthew Horton, Patrick Huck, Donny Winston, Shreyas Cholia, Shyue Ping Ong (Eds.), The Materials Project: Accelerating Materials Design Through Theory-Driven Data and Tools, Springer, Cham, 2018.

[26] Stefano Curtarolo, Wahyu Setyawan, Gus L.W. Hart, Michal Jahnatek, Roman V. Chepulskii, Richard H. Taylor, Shidong Wang, Junkai Xue, Kesong Yang, Ohad Levy, et al., AFLOW: An automatic framework for high-throughput materials discovery, Comput. Mater. Sci. 58 (2012) 218–226, https://doi.org/10.1016/j.commatsci.2012.02.005.

[27] Camilo E. Calderon, Jose J. Plata, Cormac Toher, Corey Oses, Ohad Levy, Marco Fornari, Natan Amir, Michael Mehl, Gus Hart, Marco Buongiorno Nardelli, et al., The AFLOW standard for high-throughput materials science calculations, Comput. Mater. Sci. 108 (2015) 233–238, https://doi.org/10.1016/j.commatsci.2015.07.019.

[28] Michael J. Mehl, David Hicks, Cormac Toher, Ohad Levy, Robert M. Hanson, Gus Hart, Stefano Curtarolo, The AFLOW Library of Crystallographic Prototypes: Part 1, Comput. Mater. Sci. 136 (2017) S1–S828, https://doi.org/10.1016/j.commatsci.2017.01.017.

[29] James E. Saal, Scott Kirklin, Muratahan Aykol, Bryce Meredig, Christopher Wolverton, Materials Design and Discovery with High-Throughput Density Functional Theory: The Open Quantum Materials Database (OQMD), Jom 65 (2013) 1501–1509, https://doi.org/10.1007/s11837-013-0755-4.

[30] Richard Tran, Xu Zihan, Balachandran Radhakrishnan, Donald Winston, Wenhao Sun, Kristin A. Persson, Shyue Ping Ong, Surface energies of elemental crystals, Sci. Data 3 (2016) 1–13, https://doi.org/10.1038/sdata.2016.80.

[31] Kamal Choudhary, Adam J. Biacchi, Supriyo Ghosh, Lucas Hale, Angela R. Hight Walker, Francesca Tavazza, High-throughput assessment of vacancy formation and surface energies of materials using classical force-fields, J. Phys.: Condens. Matter 30 (2018), 395901, https://doi.org/10.1088/1361-648X/aadaff.

[32] Georg Kresse, Jürgen Furthmüller, Efficiency of ab-initio total energy calculations for metals and semiconductors using a plane-wave basis set, Comput. Mater. Sci. 6 (1996) 15–50, https://doi.org/10.1016/0927-0256(96)00008-0.

[33] John P. Perdew, Kieron Burke, Matthias Ernzerhof, Generalized gradient approximation made simple, Phys. Rev. Letters 77 (1996) 3865, https://doi.org/10.1103/PhysRevLett.77.3865.

[34] Dmitry A. Aksyonov, Stanislav S. Fedotov, Keith J. Stevenson, Andriy Zhugayevych, Understanding migration barriers for monovalent ion insertion in transition metal oxide and phosphate based cathode materials: A DFT study, Comput. Mater. Sci. 154 (2018) 449–458, https://doi.org/10.1016/j.commatsci.2018.07.057.

[35] Wenhao Sun, Gerbrand Ceder, Efficient creation and convergence of surface slabs, Surf. Sci. 617 (2013) 53–59, https://doi.org/10.1016/j.susc.2013.05.016.

[36] Georg Wulff, XXV. Zur frage der geschwindigkeit des wachsthums und der auflösung der krystallflächen, Zeitschrift für Kristallographie-Crystalline Materials 34 (1901) 449–530, https://doi.org/10.1524/zkri.1901.34.1.449.

[37] Joseph H. Montoya, Kristin A. Persson, A high-throughput framework for determining adsorption energies on solid surfaces, npj Comput. Mater. 3 (2017), 14, https://doi.org/10.1038/s41524-017-0017-z.

[38] Lei Wang, Thomas Maxisch, Gerbrand Ceder, Oxidation energies of transition metal oxides within the GGA+U framework, Phys. Rev. B 73 (2006), 195107, https://doi.org/10.1103/PhysRevB.73.195107.

[39] Rico Friedrich, Demet Usanmaz, Corey Oses, Andrew Supka, Marco Fornari, Marco Buongiorno Nardelli, Cormac Toher, Stefano Curtarolo, Coordination corrected ab initio formation enthalpies, npj Comput. Mater. 5 (2019) 59, https://doi.org/10.1038/s41524-019-0192-1.

[40] Bernardo N Cacciapuoti, Emilio Segré, Radioactive isotopes of element 43, Phys. Rev. 52 (1937) 1252, https://doi.org/10.1103/PhysRev.52.1252.3.

[41] David Sholl, Janice Steckel. Density functional theory: a practical introduction, John Wiley & Sons, Inc., 2011.

[42] Nadezhda N. Kiselyova, Victor A. Dudarev, Mikhail A. Korzhuyev, Database on the bandgap of inorganic substances and materials, Inorganic Mater.: Appl. Res. 7 (2016) 34–39, https://doi.org/10.1134/S2075113316010093.

[43] Zhendong Lei, Jing Zhan, Liang Tang, Yong Zhang, Yong Wang, Recent Development of Metallic (1T) Phase of Molybdenum Disulfide for Energy Conversion and Storage, Adv. Energy Mater. 8 (2018) 1703482, https://doi.org/10.1002/aenm.201703482.

[44] F.J. Morin, Oxides Which Show a Metal-to-Insulator Transition at the Neel Temperature, Phys. Rev. Letters 3 (1959) 34, https://doi.org/10.1103/PhysRevLett.3.34.

[45] John B. Goodenough, The two components of the crystallographic transition in VO_2, J. Solid State Chem. 3 (1971) 490–500, https://doi.org/10.1016/0022-4596(71)90091-0.

[46] Issam Mjejri, Noureddine Etteyeb, Sayda Somrani, Faouzi Sediri, Tetragonal pencil-like VO_2(R) as electrode materials for high-performance redox activities, Ceram. Int. 42 (5) (2016) 6121–6128, https://doi.org/10.1016/j.ceramint.2015.12.173.

[47] Chenguang Guo, Hui Li, Wei Zhao, Jie Pan, Tianquan Lin, Xu Jijian, Mingwei Chen, Fuqiang Huang, High-quality single-layer nanosheets of MS_2 (M = Mo, Nb, Ta, Ti) directly exfoliated from AMS_2 (A = Li, Na, K) crystals, J. Mater. Chem. C 5 (2017) 5977–5983, https://doi.org/10.1039/C7TC00838D.

[48] Jung-tak Jang, Sohee Jeong, Jung-wook Seo, Min-Cheol Kim, Eunji Sim, Oh. Yuhong, Seunghoon Nam, Byungwoo Park, Jinwoo Cheon, Ultrathin zirconium disulfide nanodiscs, J. Am. Chem. Soc. 133 (2011) 7636–7639, https://doi.org/10.1021/ja200400n.

[49] Gang Wang, Xiangchao Ma, Baibiao Huang, Hefeng Cheng, Zeyan Wang, Jie Zhan, Xiaoyan Qin, Xiaoyang Zhang, Ying Dai, Controlled synthesis of Ag_2O microcrystals with facet-dependent photocatalytic activities, J. Mater. Chem. 22 (2012) 21189–21194, https://doi.org/10.1039/C2JM35010F.

[50] Jibin Chen, Huinan Che, Kai Huang, Chunbo Liu, Weidong Shi, Fabrication of a ternary plasmonic photocatalyst CQDs/Ag/Ag_2O to harness charge flow for photocatalytic elimination of pollutants, Appl. Catal. B: Environ. 192 (2016) 134–144, https://doi.org/10.1016/j.apcatb.2016.03.056.

[51] Workneh M. Shume, H. C. Ananda Murthy, Enyew Amare Zereffa, A review on synthesis and characterization of ag2o nanoparticles for photocatalytic applications, J. Chem. 2020 (2020), https://doi.org/10.1155/2020/5039479.
[52] Junwu Zhu, Dan Li, Haiqun Chen, Xujie Yang, Lu Lude, Xin Wang, Highly dispersed CuO nanoparticles prepared by a novel quick-precipitation method, Mater. Lett. 58 (2004) 3324–3327, https://doi.org/10.1016/j.matlet.2004.06.031.
[53] Masood Sahooli, Samad Sabbaghi, Rahmatallah Saboori, Synthesis and characterization of mono sized CuO nanoparticles, Mater. Lett. 81 (2012) 169–172, https://doi.org/10.1016/j.matlet.2012.04.148.
[54] Chenguang Guo, Hui Li, Wei Zhao, Jie Pan, Tianquan Lin, Xu Jijian, Mingwei Chen, Fuqiang Huang, High-quality single-layer nanosheets of MS_2 (M = Mo, Nb, Ta, Ti) directly exfoliated from AMS_2 (A = Li, Na, K) crystals, J. Mater. Chem. C 5 (2017) 5977–5983, https://doi.org/10.1039/C7TC00838D.
[55] Thomas A. Mellan, Ricardo Grau-Crespo, Density functional theory study of rutile VO_2 surfaces, J. Chem. Phys. 137 (2012), 154706, https://doi.org/10.1063/1.4758319.
[56] Troy D. Manning, Ivan P. Parkin, Atmospheric pressure chemical vapour deposition of tungsten doped vanadium(IV) oxide from $VOCl_3$, water and WCl_6, J. Mater. Chem. 14 (2004) 2554–2559, https://doi.org/10.1039/B403576N.
[57] Woanseo Park, Juhun Park, Jingon Jang, Hyungwoo Lee, Hyunhak Jeong, Kyungjune Cho, Seunghun Hong, Takhee Lee, Oxygen environmental and passivation effects on molybdenum disulfide field effect transistors, Nanotechnology 24 (2013), 095202, https://doi.org/10.1088/0957-4484/24/9/095202.
[58] Jana Martincová, Michal Otyepka, Petr Lazar, Is single layer MoS2 stable in the air? Chem.-A Eur. J. 23 (2017) 13233–13239, https://doi.org/10.1002/chem.201702860.
[59] Raghavan Rakhi, Doddahalli Nagaraju, Pierre Beaujuge, Husam Alshareef, Supercapacitors based on two dimensional VO2 nanosheet electrodes in organic gel electrolyte, Electrochimica Acta 220 (2016) 601–608, https://doi.org/10.1016/j.electacta.2016.10.109.
[60] Ziyauddin Khan, Baskar Senthilkumar, Sung Park, Seungyoung Park, Juchan Yang, Jeong Hyeon Lee, Kon Hyun-Song, Youngsik Kim, Sang Kwak, Hyunhyub Ko, Carambola-shaped VO2 nanostructures: a binder-free air electrode for an aqueous na-air battery, J. Mater. Chem. A 5 (2017) 2037–2044, https://doi.org/10.1039/C6TA09375B.
[61] Qiunan Liu, Tingting Yang, Du. Congcong, Yongfu Tang, Yong Sun, Peng Jia, Jingzhao Chen, Hongjun Ye, Tongde Shen, Qiuming Peng, et al., In situ imaging the oxygen reduction reactions of solid-state Na-O2 batteries with CuO nanowires as the air cathode, Nano Lett. 18 (2018) 3723–3730, https://doi.org/10.1021/acs.nanolett.8b00894.
[62] Ke-Jing Huang, Lan Wang, Ji-Zong Zhang, Ke Xing, Synthesis of molybdenum disulfide/carbon aerogel composites for supercapacitors electrode material application, J. Electroanal. Chem. 752 (2015) 33–40, https://doi.org/10.1016/j.jelechem.2015.06.005.
[63] Jungwook Woo, Eun Seob Sim, Minyeong Je, Heechae Choi, Yong-Chae Chung, Theoretical dopant screening and processing optimization for vanadium disulfide as cathode material for li-air batteries: A density functional theory study, Appl. Surf. Sci. 508 (2020), 145276, https://doi.org/10.1016/j.apsusc.2020.145276.
[64] Xu Jun Feng, Changzheng Wu Sun, Lele Peng, Chenwen Lin, Hu Shuanglin, Jinlong Yang, Yi Xie, Metallic few-layered VS2 ultrathin nanosheets: high two-dimensional conductivity for in-plane supercapacitors, J. Am. Chem. Soc. 133 (2011) 17832–17838, https://doi.org/10.1021/ja207176c.
[65] Shidong Ji, Yangang Zhao, Feng Zhang, Ping Jin, Synthesis and phase transition behavior of W-doped VO_2(A) nanorods, J. Ceram. Soc. Jpn. 118 (2010) 867–871, https://doi.org/10.2109/jcersj2.118.867.